Article

Band Gap Modulation in Zn_2TiO_4 Spinels for Efficient UV-A Persistent Luminescence

Ankit Sharma [1], **Moondeep Chouhan** [2] **and Suchinder K. Sharma** [1,*]

1 Amity School of Physical Sciences, Amity University Punjab, IT City, Sector-82A, Mohali 140306, India; ankitkush442@gmail.com
2 Central Instrumental Laboratory, Amity University Punjab, IT City, Sector-82A, Mohali 140306, India; moondeepc@pb.amity.edu
* Correspondence: suchindersharma@gmail.com; Tel.: +91-172-520-3544

Abstract: Spinels are important materials for an application in bioimaging. The key advantage with spinel-type hosts is the presence of antisite defects, which act as charge reservoirs for trapping electrons and holes at complementary defect sites. This makes them a host system similar to a molecular system. Herein, we present a systematic approach to modulating the band gap of an inverse Zn_2TiO_4 spinel. With a change in ZnO concentration, the absorption band at 375 nm diminishes and disappears at a $ZnO:TiO_2$ concentration of 1.40:1.00. The band gap of the material is modified from 3.30 to 4.40 eV. The crystal structure of the sample does not change drastically as determined using X-ray diffraction and Rietveld refinement. The Zn_2TiO_4 emits in the UV-A region with a lifetime in the time domain of 'ns'. The sample also shows persistent luminescence of at least 15 min upon excitation with 254 nm with prominent emission in the UV-A region (300–390 nm). The present results open a new avenue for the synthesis of spinel hosts where the band gap can be modified with ease. The UV emission thus observed is expected to find usage in interesting applications like photocatalysis, anti-counterfeiting, water disinfecting, etc.

Keywords: spinel; bioimaging; UV emission; phosphor; band gap

1. Introduction

Optical materials with a spinel-type structure have attracted researcher's interest in the past ten years due to the possibility of using Cr^{3+}-doped samples for an interesting application of bioimaging. Since the first report on an application of a zinc gallate spinel for bioimaging by Maldiney et.al. [1], several other hosts from the same (or similar) spinel family have been explored extensively. The research in this direction was extended from imaging probes sensitive in the near infrared (NIR) region around 700 nm (also known as the first biological window) to higher second and/or third biological windows lying deep in the wavelength domain. The important point in all these investigations was to synthesize hosts with crystal fields that can affect the Cr ions (present as dopants) in such a way that there is a shift in the emission maximum from the NIR to a higher wavelength region. This strategy was reported for a magnesium gallate host where the Cr emission shifted to 712 nm as compared to 693 nm for a zinc gallate host [2]. The technological key point of spinels that makes them suitable for such an application is the presence of antisite defects in the host lattice. Antisite defects make it possible for the dopant ion to sit at a distorted site as compared to the actual site where the ion is expected to be present in the host lattice.

Spinels can be categorized as normal spinels, which have the general formula of AB_2O_4, and an inverse spinels, which have a general formula, $B(AB)O_4$. Another class of spinels is complex spinels, which have a mixture of normal and inverse spinels. In recent reports, spinels have also found technological importance as suitable materials for magnetic [3], high-temperature ceramics [4], as superhard materials [5], and as materials suitable for high

pressure sensing applications [6]. The common synthesis procedure of spinel-type materials is a solid-state method. The materials in this procedure are synthesized at high temperatures under a reductive or inert atmosphere. Such an environment is required to keep the host and dopant in the desired valence state, for example, +3 for Cr. From the literature, one can also observe that most of the researchers' work on normal spinel-type materials, while very little, is published on inverse spinels, probably due to complex synthesis conditions. Another important observation is the recent developments of researchers on UV-emitting persistent luminescent (PersL) materials. UV-emitting PersL materials have found application in anticounterfeiting, photocatalysis, photodynamic therapy, and others, as discussed in a recent review article [7]. The UV region can be sub-categorized as UV-A, UV-B, and UV-C regions, and some smart techniques are required to prepare such materials.

Based on these two aspects, in the present work, we investigated the influence of synthesis conditions, annealing temperature and ZnO concentration in zinc orthotitanate (Zn_2TiO_4). Zn_2TiO_4 is an inverse spinel that exhibits interesting dielectric and optical properties, making it potentially useful in electronics, photonics, and optoelectronics [8–11]. A Zn_2TiO_4 application for photocatalysis involves light to drive chemical reactions, which can be used for environmental remediation and water purification [11]. It has a band gap of 3.30 eV (375 nm) with a prominent photoluminescence (PL) emission in the wavelength region of 470–800 nm [12]. The 375 nm band also corresponds to ZnO-related host band gap. Hence, based on this overview and these objectives, we prepared twelve samples using the solid-state synthesis method, modulating the ZnO concentration with the objective to alter the ZnO-related absorption band at 375 nm or to modify the Zn_2TiO_4 band gap. During the initial annealing of samples between temperatures of 700 and 1000 °C, we observed that for the sample annealed at 800 °C with a $ZnO:TiO_2$ concentration of 2.00:1.00, Zn_2TiO_4-related diffraction peaks could be obtained. We modulated the ZnO concentration first with a decrease in small steps of 0.02 to 0.06 mol in comparison to the TiO_2 ratio, and later, in comparably larger steps of 0.20 to 1.00 mol, to optimize the absorption band related to ZnO. The UV-Visible diffuse reflectance spectra were obtained for all the samples to understand the variation in the band gap of all the samples. The results indicate a clear deviation in band gap from 3.30 eV to 4.40 eV for a sample with $ZnO:TiO_2$ concentration of 1.40:1.00. Photoluminescence and luminescence decay studies were performed on a phase-pure sample to determine the recombination process and lifetime of charges in their excited state. The optimized sample showed PersL in the wavelength region of 300–390 nm with a decay time of at least 10 min.

2. Materials and Methods

2.1. Synthesis

All the samples were prepared using the solid-state synthesis method. ZnO (Himedia, Mumbai, India, purity > 99%) and TiO_2 (Himedia, India, purity > 99%) were used as precursors. Appropriate amounts of the precursors were mixed in an agate mortar for 30 min, and a pellet with a 13 mm diameter was prepared using hydraulic press with a pressure of 10 ton. Initially, four different pellets were sintered in a muffle furnace at temperatures of 700 °C, 800 °C, 900 °C and 1000 °C for two hours each in an air atmosphere. Later, these pellets were crushed in an agate mortar and used as is for further characterization. Another eight samples of Zn_2TiO_4 were synthesized with different concentrations of ZnO at 800 °C temperature (2 h each). All the samples were calcined in the air atmosphere, and no special/reductive/inert conditions were used for the synthesis. The details of the samples prepared and their respective codes are presented in Table 1.

Table 1. The list of all the twelve samples prepared during the course of the work. The annealing time for all the samples was fixed at 2 h.

Sample No	Sample Code	ZnO:TiO$_2$	Temperature (°C)
1.	A01	2.00:1.00	700
2.	A02	2.00:1.00	800
3.	A03	2.00:1.00	900
4.	A04	2.00:1.00	1000
6.	A06	1.96:1.00	800
7.	A07	1.94:1.00	800
8.	A08	1.80:1.00	800
9.	A09	1.60:1.00	800
10.	A10	1.40:1.00	800
11.	A11	1.20:1.00	800
12.	A12	1.00:1.00	800

2.2. Characterization

The phase purity (crystallinity) of all the samples was determined by measuring powder X-ray diffraction (pXRD) patterns on a Rigaku instrument with model MiniFlex 600, having Cu-target emitting K$_\alpha$ radiations (wavelength = 1.54060 Å). The scan speed for obtaining diffraction patterns was fixed at 0.01°/s over a wide range of 2θ angle from 10 to 90°. The refinement of the crystal structure was performed using FullProf Suite software (Version 8.00) [13]. The diffuse reflectance spectra were measured in the UV-Visible wavelength range of 200–900 nm, on a Shimazdu spectrophotometer, Kyoto, Japan model 2600i. A Halogen lamp (Model No. 64604) and a deuterium lamp (Model No. L6380) were used for their light emission in the visible and UV regions within spectrophotometer, respectively. An integrating sphere and BaSO$_4$ were used for baseline correction, with measurements performed in reflectance mode. The micrographs of the as-prepared samples were studied using a field emission scanning electron microscope (FE-SEM) from Hitachi Japan Instruments with model no. SU-8010. The purity and elemental composition of the as-prepared samples (A02 and A10) were verified by energy dispersive X-ray spectroscopic analysis (EDS; Quantax XFlash®6|30, Bruker Quantax). A Nicolet™ Summit LITE spectrometer from Thermo Fisher Scientific (Waltham, MA, USA), was used to measure Fourier transform infrared (FTIR) spectra of different samples in the wavenumber range of 400–4000 cm^{-1}. The samples were mixed with KBr to prepare pellets of 8 mm diameter. The PL excitation and emission spectra were measured on a Fluoromax Plus-C spectrofluorometer from Horiba Scientific (Kyoto, Japan). The spectra were measured using an R928P photon counting photomultiplier tube with a wavelength detection limit of 185–850 nm. The data were corrected for the lamp input and optics used. Luminescence decay measurements were performed on a time-correlated single photon counting-multichannel scaling system (TCSPC-MCS) with pulsed excitation using a Deltadiode™ DD-260 model (Serial No. 18591) with an emission maximum at a wavelength of 265 nm. Thermoluminescence (TL) and PersL were measured on Nucleonix TL1009 reader (Telangana, India). The TL measurements were performed at a linear heating rate of 1 K/s, with excitation performed using an 8 W 254 nm UV tube procured from Phillips (Amsterdam, The Netherlands).

3. Results

The present work represents a systematic approach to modulate the ZnO concentration in Zn$_2$TiO$_4$ with the objective of changing the band gap of the matrix.

3.1. Effect of Annealing Temperature

Four samples were prepared by annealing the stoichiometric amount of ZnO and TiO$_2$ in a ratio of 2.00:1.00 at different temperatures between 700 and 1000 °C (100 °C each). The pXRD pattern of the four samples is shown in Figure 1a,b. The standard powder diffraction pattern from the Crystallographic Open Database (COD) with file no. 1544562 is also shown

for comparison (marked standard). When the sample is calcined at 700 °C (Sample A01), several reflections are obtained which cannot be assigned to Zn_2TiO_4 alone and can thus be considered as a mix of several intermediate crystalline phases [cf. Figure 1b]. However, when the samples are calcined at 800 °C or at higher temperatures up to 1000 °C (samples A02 to A04), the prominent reflections match closely with the standard file, cf. Figure 1a,b. A very small amount of unreacted ZnO in the host lattice is also observed, as marked at 31.75 and 36.25 2θ values in Figure 1b. However, the prominent crystallographic lines correspond to Zn_2TiO_4 only.
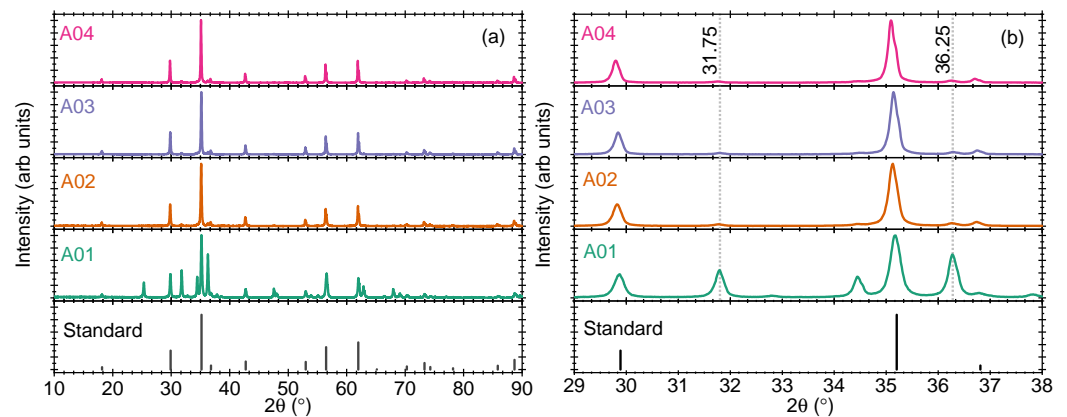
Figure 1. (**a**) The pXRD pattern of four samples annealed at different temperatures; (**b**) zoom-in showing extra peaks of small intensity at 31.75 and 36.25 2θ degrees which corresponds to ZnO.

3.2. Change of ZnO Concentration from 2.00:1.00 → 1.94:1.00

As a first step to modulate the band gap of Zn_2TiO_4, we optimize the ZnO concentration in small steps to 1.98:1.00 (sample A05), 1.96:1.00 (sample A06), and 1.94:1.00 (sample A07). The pXRD results of the three samples are shown in Figure 2a,b. The reason for this choice is the already reported impact of such modification on the crystallinity of the samples and the improvement of the persistent luminescence properties of doped $ZnGa_2O_4$ samples [1,2]. Looking at the results in Figure 2a, the positions of the prominent diffraction peaks remain the same in all samples, suggesting that the prominent crystal structure is not distorted upon a small change in the ZnO concentration. However, a decrease in the reflection intensity of unreacted ZnO-related peaks is clearly noticed. A reflection at 31.75 2θ values is shown in Figure 2b for better visualization of this inference. The effect of such modification on the UV-Vis absorption bands (or band gap) is discussed in later sections.
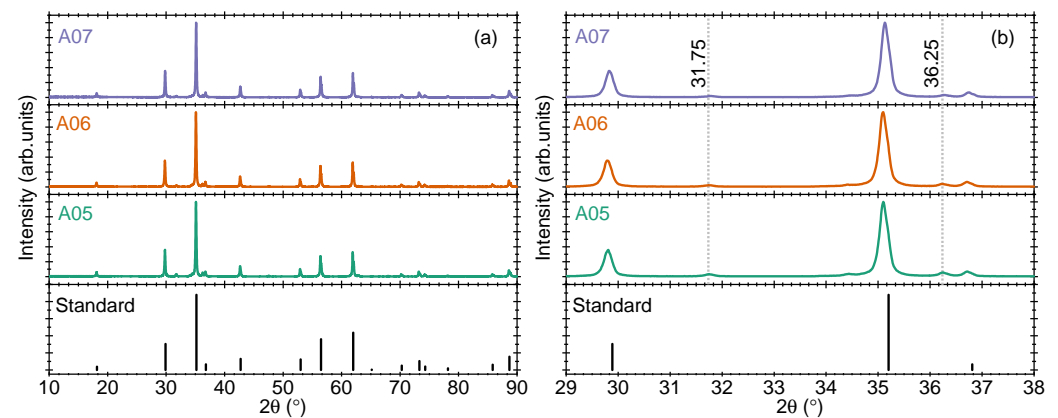
Figure 2. (**a**) pXRD pattern of three samples with ZnO:TiO$_2$ ratio of 1.98:1.00, 1.96:1.00 and 1.94:1.00 annealed at temperature 800 °C; (**b**) zoom-in showing extra peaks of small intensity of ZnO.

3.3. Change of ZnO Concentration with a 0.20 Step Size

Considering that there is very little change in the ZnO-related reflections in our samples and no change in prominent Zn_2TiO_4-related reflections, we optimized the ZnO ratio in a comparably larger step of 1.80:1.00 (samples A08), 1.60:1.00 (sample A09), and 1.40:1.00 (sample A10). The results of the three samples are shown in Figure 3a,b. Interestingly, the prominent small peaks that were obtained in Sections 3.2 and 3.3, for example, at 31.75 2θ degrees, are not obtained now. Instead, a new reflection at 32.75 2θ degree is observed. This reflection was also observed in sample A01, cf. Figure 1a,b. The origin of the two reflections cannot be the same as they are obtained at different experimental conditions. While looking into the literature, we observe that the reflection at 31.75 2θ degrees is due to ZnO in wurtzite phase, while the 32.75 2θ degrees reflection is due to zinc blende-type ZnO [14]. This new reflection can also be associated with $Zn_2Ti_3O_8$ phase. However, the position of Zn_2TiO_4 related reflections is unaffected by the change in ZnO concentration up to sample A10.
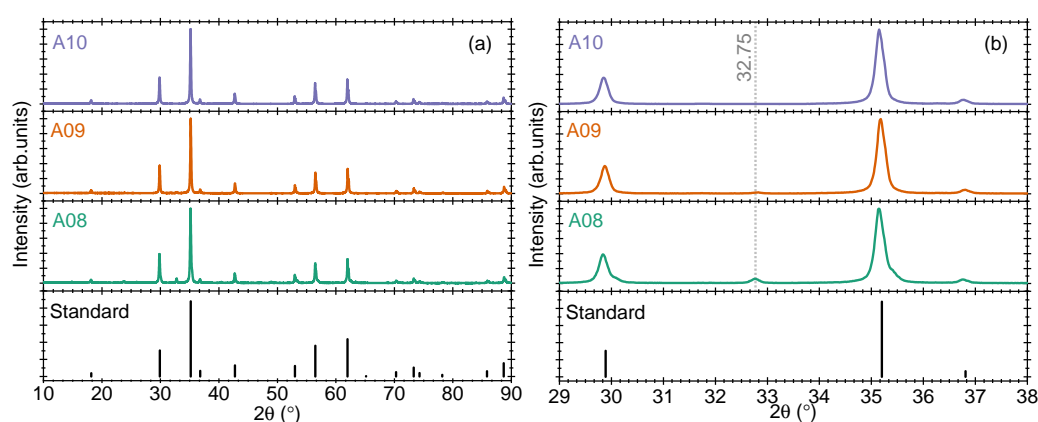

Figure 3. (**a**) pXRD pattern of three samples with $ZnO:TiO_2$ concentration of 1.80:1.00, 1.60:1.00 and 1.40:1.00, annealed at a temperature 800 °C (2 h); (**b**) zoom-in of new reflections of ZnO peaking at 32.75 2θ degrees.

To further understand the effect of a decrease in the concentration ratio of the two precursors, the amount of ZnO is decreased to 1.20:1.00 (sample A11) and 1.00:1.00 (sample A12). For these samples, several additional reflections are observed in the pXRD pattern (results not shown). These additional reflections are present due to a mix of several phases from the $ZnO-TiO_2$ family. As the present work focuses on Zn_2TiO_4 synthesis and its optimization, we choose to continue our investigations on samples with codes between A01-A10 only. As an important observation from the present results, we infer that sample A10 with $ZnO:TiO_2$ concentration of 1.40:1.00 gives optimized pXRD results where the reflections due to unreacted ZnO vanish, while the main reflections due to Zn_2TiO_4 are conserved.

3.4. Rietveld Refinement of Sample A10

The Rietveld refinement of sample A10 was performed to determine the purity of the sample. The results after fitting the pXRD pattern are shown in Figure 4a. When the experimental and calculated patterns are evaluated for an overlap between the two, a good correlation is observed. The data could be fitted with $\chi^2 = 0.14$. The cell parameters are calculated as: $a = b = c = 8.4721(5)$ Å; $\alpha = \beta = \gamma = 90°$. The volume of the unit cell is calculated as $V = 608.0975(7)$ Å^3. When the cell parameters are compared with the standard data, a small change in the lattice parameters is noticed, Δa, Δb, Δc, $\Delta V < 1\%$, which suggests that the ZnO concentration-optimized sample is of high purity.
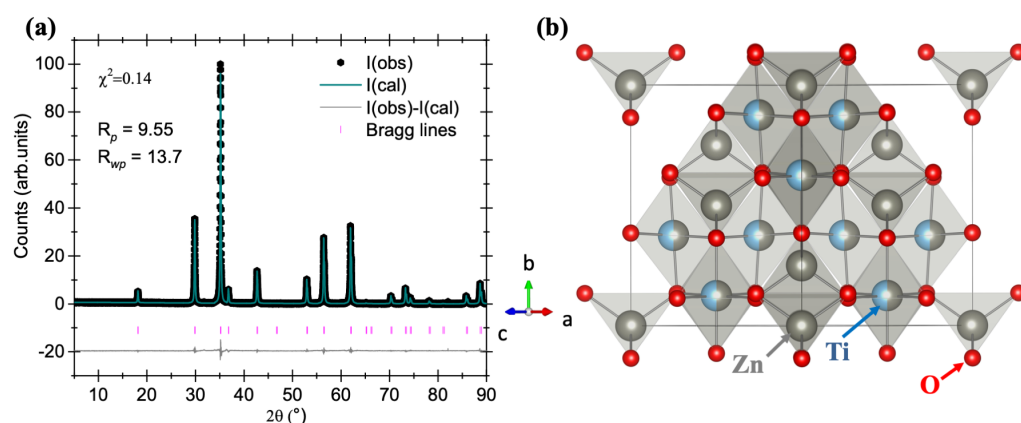
Figure 4. (**a**) Experimental and fitted pXRD pattern of sample A10, and (**b**) a representative crystal structure of Zn_2TiO_4.

Zn_2TiO_4 has a cubic spinel structure with the space group Fd–3m (#227). In the structure, the Zn^{2+} cations occupy the 8a and 16d sites, Ti^{4+} cations occupy the 16d sites, and O^{2-} occupies the 32e site. The representative crystal structure is shown in Figure 4b. In the crystal structure of Zn_2TiO_4, Zn(1) occupies the tetrahedral site, while Zn(2)-Ti together occupy the octahedral site. The present host can also be written as $Zn[ZnTi]O_4$ [15]. We wish to mention here that despite a change in the expected concentration ratio of $ZnO:TiO_2$ from 2.00:1.00 to 1.40:1.00, no major changes in the crystallographic reflections of Zn_2TiO_4 are observed, and only reflections due to unreacted ZnO diminish.

3.5. FE-SEM Analysis

The morphology and grain size distribution of the prepared samples are determined using FE-SEM analysis. The results of the samples A01 to A04, and A10 are shown in Figure 5a–e. For all the samples between A01 to A04, larger grain particles (size > 150 nm) are obtained along with little contribution of grains with comparatively smaller size (size < 150 nm), cf. Figure 5a–d. However, the results of sample A10 show mostly larger grains (size > 150 nm), cf. Figure 5e. This suggests that the ZnO impurity detected in our pXRD results of samples A01 to A04 has a smaller grain size when compared to grains that belongs to the Zn_2TiO_4 host (sample A10). This is also evident when Figure 5a and Figure 5b or Figure 5e are compared, where in the first case, the grains have a comparably lower size distribution ($\sim$144 nm) and are dominated by the presence of ZnO in the pXRD pattern. For the four samples, an increase in the grain size is observed with a value of $\sim$144 nm for sample A01, $\sim$163 nm for sample A02, $\sim$217 nm for sample A03, and $\sim$253 nm for sample A04.

This observation is in expected lines as with an increase in the annealing temperature, the crystallinity and grain size are expected to increase. The reason for such a change in the grain size can be attributed to the re-crystallization process. It is also possible that there is a decrease in the deformation and grain boundaries at high temperatures. More interestingly, when the grain size of samples A02 and A10 are compared, both the samples possess a similar grain size of $\sim$163 nm, suggesting that the modulation of the concentration of ZnO has no impact on the grain size of Zn_2TiO_4.

The purity and elemental composition of the as-prepared samples were further verified by energy dispersive X-ray spectroscopic (EDS) analysis, as shown in Figure 5f,g. The EDS spectrum of the selected image shows the peaks of zinc (K_α = 8.6 keV), L_α = 1.0 keV), titanium (K_α = 4.5 keV, K_β = 4.9 keV), and oxygen (K_α = 0.5 keV). The EDS semi-quantitative analysis of sample A02 indicates atomic percentages of 30.99% for zinc and 14.98% for titanium, resulting in an atomic ratio of 2.06:1.00 in comparison to the expected value of 2.00:1.00 used during synthesis (see Table 1). Sample A10 shows atomic percentages of 26.25% for zinc and 19.14% for titanium, resulting in an atomic ratio of 1.39:1.00 in

comparison to the expected value of 1.40:1.00 (see Table 1). It is also to be mentioned here that the Rietveld refinement suggested that sample A10 is the best sample where no additional signatures of unreacted ZnO are observed.
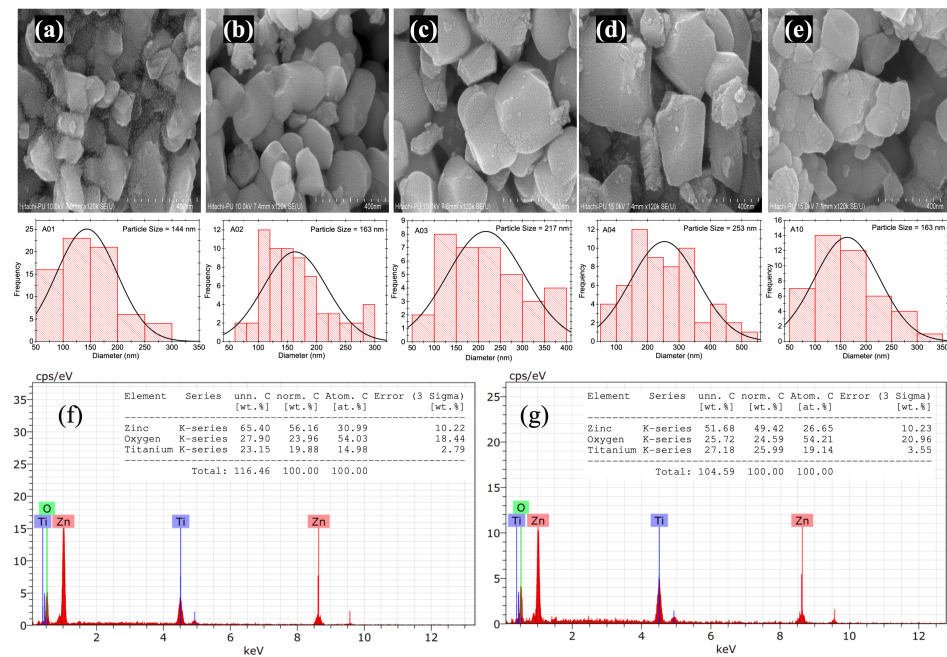
Figure 5. (**a**–**e**) FE-SEM micrographs for different samples at different temperatures, i.e., 700, 800, 900, 1000 °C and 800 °C, respectively; (**f**) EDS spectra of sample A02, and (**g**) EDS spectra of sample A10. The relative compositions for the two samples are shown in the inset of (**f**,**g**).

3.6. UV–Vis Diffuse Reflectance

The diffuse reflectance spectra of all the samples are shown in Figure 6a–c. The spectra can be categorised into three domains: (a) as a function of temperature as per the discussion in Section 3.1 of samples A01–A04 (Figure 6a); (b) as a function of small change in ZnO concentration as discussed in Section 3.2 for samples A05 to A07 (Figure 6b); and (c) as a function of large change in ZnO concentration as discussed in Section 3.3 for samples A08 to A10 (Figure 6c). The results of sample A02 are also shown in all three graphs for comparison.
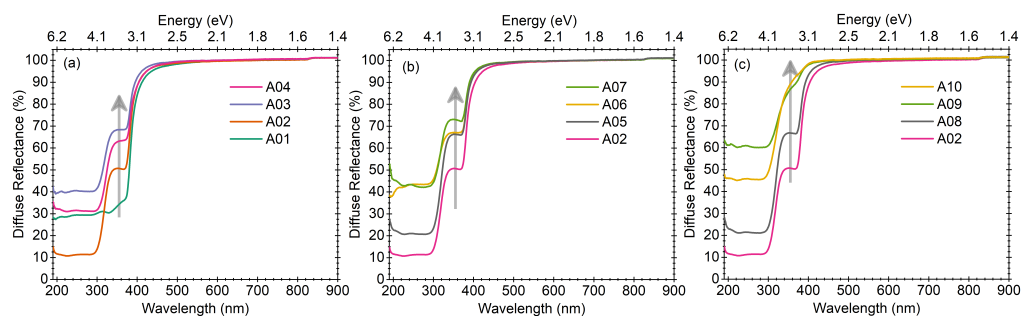
Figure 6. The UV-Vis-NIR patterns for samples containing different temperatures and concentrations of ZnO for samples, (**a**) A1 to A4; (**b**) A2 and A5 to A7; and (**c**) A2 and A8 to A10.

For sample A01, the UV-Visible diffuse reflectance spectra show a single broad absorption with a maximum at ∼375 nm. In this sample, we noticed several reflections in the pXRD pattern. For samples A02 to A04, the main UV-Visible absorption maximum is observed at 300 nm along with a shoulder at ∼375 nm. Upon decreasing the ZnO concentration in small steps [Figure 6a], the major change is observed in the 375 nm band,

whose intensity decreases with a decrease in the ZnO concentration. The present UV-Visible diffuse reflectance results are in good agreement with the pXRD patterns, where similar observations could be made. Similar results are obtained when the ZnO concentration decreases in larger steps [Figure 6c]. We observe that the intensity of the shoulder peak at 375 nm decreases and is almost negligible for sample A10, similar to the pXRD pattern. The pXRD and UV-Vis reflectance results are found to be in good agreement with each other.

When we investigate the literature for information regarding the type of bandgap of Zn_2TiO_4, we observe varied information. In ref. [16] on Zn_2TiO_4 films, the material is mentioned to be a direct band gap semiconductor with an optical band gap energy of 3.09 eV (400 nm). However, in another article, it is mentioned to be indirect in nature with an optical band gap of 3.29 eV (376 nm) [17]. In our results, we also observe a band at 375 nm similar to these reports. However, this band disappears when the concentration of ZnO decreases, suggesting that the band gap can be modulated without affecting the crystallinity of the host matrix. In one of the articles by Zhang et al. [18], it is mentioned that the band gap of Zn_2TiO_4 with the highest crystal quality is 4.41 eV (282 nm). When we compare this observation with our results, where we also obtain a band gap maximum in the same wavelength region for sample A10, we infer that the band gap of Zn_2TiO_4 could be ~4.40 eV, and the band at 3.30 eV as reported in earlier findings could be a result of unreacted ZnO in the host lattice.

3.7. Fourier Transform Infrared (FTIR) Spectroscopy

Figure 7 shows FTIR spectra of samples A01 to A04 and A10. The samples are measured in the transmission mode within the wavenumber region of 400–4000 cm^{-1}. The signatures are observed with maximum transmittance (or absorption) at ~585 cm^{-1}, ~1635 cm^{-1}, ~2365 cm^{-1}, ~2856 cm^{-1}, ~2930 cm^{-1}, and ~3430 cm^{-1} for all the samples. The band at 585 cm^{-1} is due to stretching vibration in the TiO_6 group, while the band around 1635 cm^{-1} is attributed to Zn-O bond formation. The third signature around 2365 cm^{-1}, which is observed in four samples only, is attributed to the artifact caused by the spectrometer, in accordance with the earlier report by Leen et al. [19]. We also observed a similar signature in our recent results on $CaZrO_3$ samples [20]. The origin of FTIR spectra at 2856 and 2930 cm^{-1} is unclear at this stage. The broad band with a maximum at 3430 cm^{-1} is due to the presence of molecular water in Zn_2TiO_4. It is observed that despite annealing at 1000 °C, the samples show the presence of water in the lattice, suggesting that the water is absorbed by the samples from the air and is hygroscopic in nature. No major difference in the FTIR spectra of samples A02 and A10 is observed, as in one sample there is an excess of ZnO while the other is a ZnO-deficient Zn_2TiO_4 sample.
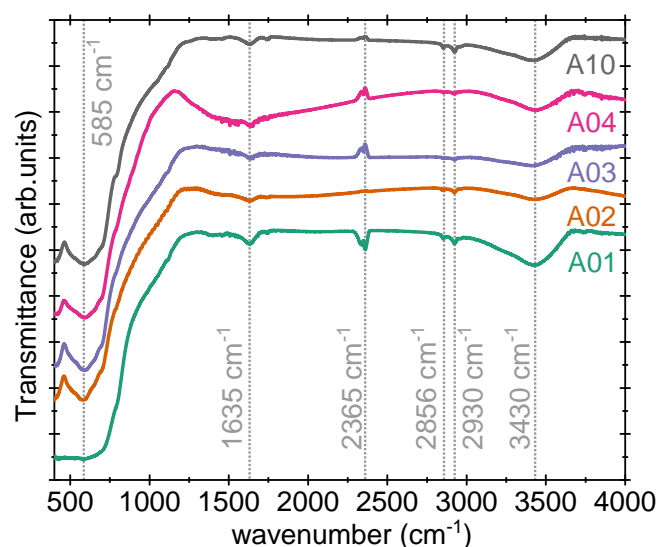

Figure 7. The FTIR transmission pattern for five different samples.

3.8. Photoluminescence (PL) Spectra

The PL excitation and emission spectra of sample A10 (pure Zn_2TiO_4) are shown in Figure 8a,b. The PL excitation spectrum contains one prominent band at 225 nm when monitored for an emission maximum at 346 nm (Figure 8a). Upon excitation at wavelengths 225, 254, and 275 nm, the emission maximum is obtained at 346 nm (Figure 8b). The excitation spectrum overlaps exactly with the UV-Vis diffuse reflectance spectrum, suggesting that the origin of the two is the same. The sample can be excited with any wavelength lower than 280 nm and needs UV-C light to produce efficient PL emission. The emission of the pure Zn_2TiO_4 sample is in the UV-A region and extends between 300 and 390 nm. For this band-to-band excitation, the origin of PL emission is anticipated to be defects similar to the ones observed in undoped $ZnGa_2O_4$ samples, where the prominent emission has been attributed to the self-activated centres of the octahedral Ga-O group in the spinel lattices [21]. While looking for information in the literature, we found a recent article that mentions the origin of PL emission in Zn_2TiO_4 to be O^{2-} and Zn^{2+} vacancies related that are present in the crystal lattice [11]. The conduction band in Zn_2TiO_4 lattice is made up of Ti-3s orbitals and the valance band is composed of Zn-3d and O-2s orbitals [22].
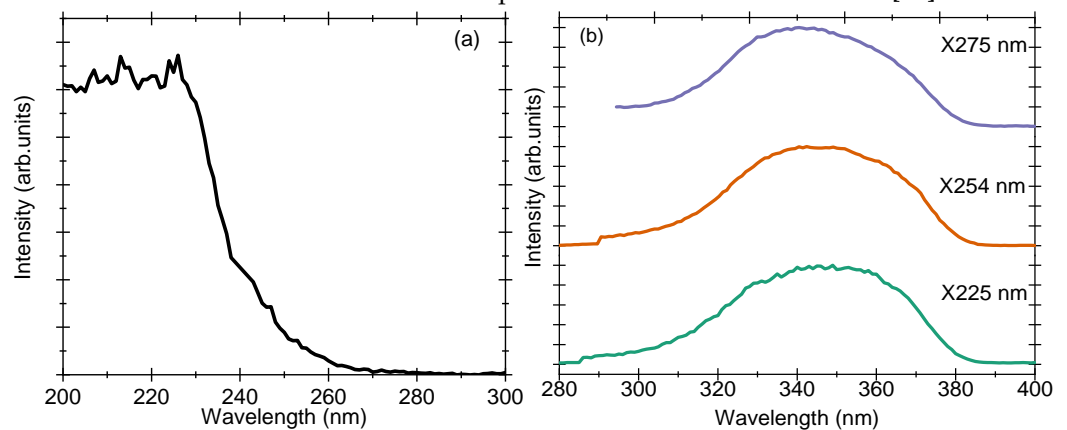
Figure 8. (**a**) PL excitation spectrum while monitoring the maximum at 346 nm, and (**b**) PL emission spectra monitored upon excitation at 225, 254, and 275 nm. The letter X in the figure denotes the excitation wavelength.

3.9. Luminescence Lifetime

The lifetime of the charges in their excited state is determined for sample A10 by measuring decay curves at the maximums of PL emission at 325 and 346 nm. The results are shown in Figure 9. The IRF signal is also presented in the figure for comparison. The excitation is performed using a pulsed source with emission at a wavelength of 265 nm. Both curves could not be fitted with a single exponential decay curve, and a double exponential curve is used to fit the curves using Equation (1).

$$y = A_1 \cdot exp(-x/t_1) + A_2 \cdot exp(-x/t_2) \tag{1}$$

where, A_1, A_2 are the amplitudes of individual exponential, and t_1 and t_2 are decay constants. The results are combined in Table 2.

Generally, when the electron is excited to a higher quantum state from where it is expected to come back to the ground state accompanied by the emission of photons due to electron–hole recombination, the intensity of emission is written as $I = I_0 exp(-t/\tau)$. The decay curve in such a case can be fitted with monomolecular or first-order decay kinetics. On the contrary, when 'n' number of electrons move to the conduction band, leaving behind 'n' number of empty centers, the rate of recombination, 'r' is given by $(-dn/dt) = r.n^2$, and the decay curve can be fitted with hyperbolic or second order decay kinetics.
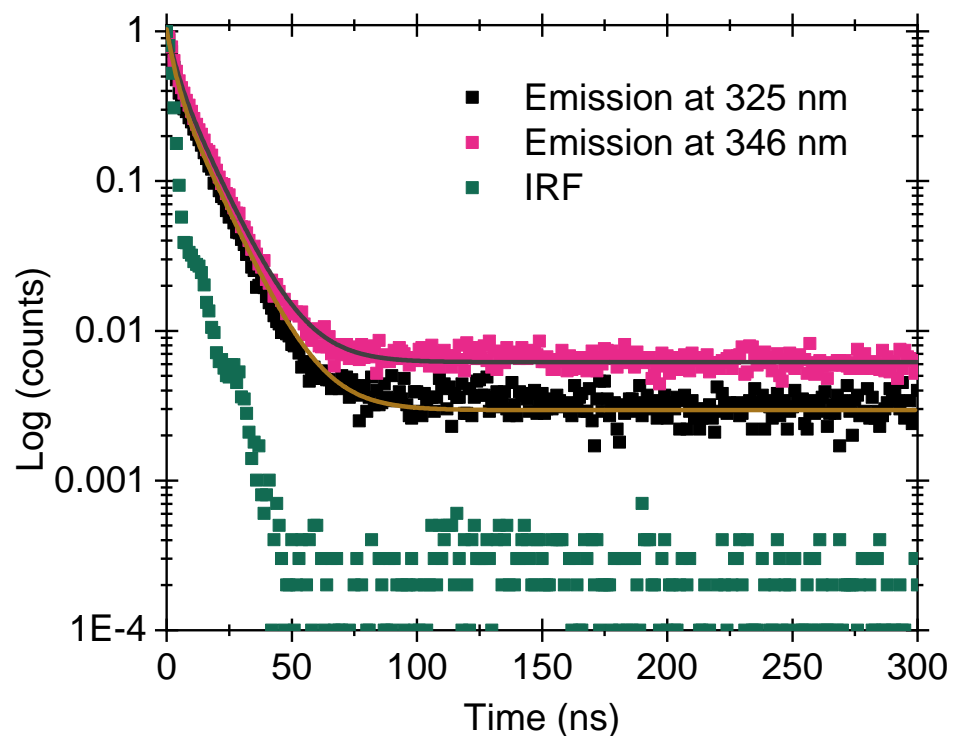
Figure 9. A Semi-log plot of decay curves measured at prominent emissions at wavelengths 325 and 346 nm is shown. The fitting of the decay curves is depicted using gray and yellow lines.

When looking into our results, there are at least two different pathways of electron relaxation from the excited state to the ground state, as is evident from the lifetime of ∼3 ns and ∼11 ns. The results also suggest that the decay follows second-order kinetics. When the decay results are compared upon excitation at 325 and 346 nm, we observe that the relaxation pathways are similar in the two cases.

Table 2. The variation of decay constants obtained after fitting luminescence decay curves in Figure 9.

Sample	Emission Wavelength (nm)	t_1 (ns)	t_2 (ns)
A10	325	3.25 ± 0.04	11.49 ± 0.28
A10	346	3.35 ± 0.11	11.61 ± 0.14

3.10. Thermoluminescence (TL) and PersL

We measured the TL and PersL of sample A10. The results are shown in Figure 10a,b. The excitation in all cases is performed using 254 nm emitting UV light for 5 min. The choice of 254 nm light was based on the PL excitation spectrum. The TL results obtained immediately (after stopping excitation) show an initial signal at room temperature followed by a maximum at 175 °C, cf. Figure 10a. The initial signal at room temperature is a clear indication of PersL in sample A10. The reason for PersL is the charge trapping and detrapping at room temperature, suggesting that room temperature provides sufficient energy for charges to become detrapped. These charges have an equal probability of becoming detrapped (and retrapped) at room temperature, producing PersL. We measured PersL at room temperature, and the results are shown in Figure 10b. The log–log plot shows that the signal decays almost linearly and reaches the background signal after 15 min of measurement time. The background signal is also shown for a comparison of the two signals. In the third measurement, we recorded TL after recording PersL (Figure 10a [green line]). In this case, the TL maximum is obtained at 225 °C. By assuming first-order kinetics and using the equation 25kT_m [23], the activation energy (E_{ac}) of the charge storing

defects is determined to be 1.07 eV. Considering an electron trap model, we infer that these defects are approximately 1.07 eV below the conduction band.
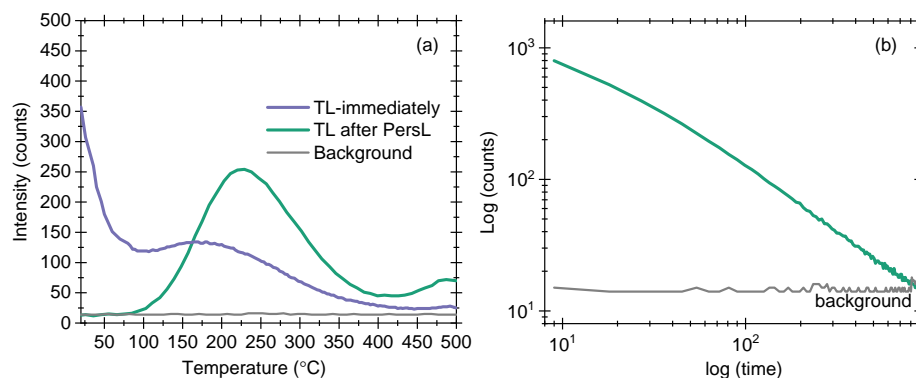
Figure 10. (**a**) TL results of sample A10 after stopping the excitation and after measuring PersL in the sample, and (**b**) log–log plot of the PersL decay curve. The background signal in TL and PersL is also shown for comparison.

4. Discussion

Zn_2TiO_4 with an inverse spinel crystal structure appears to be an interesting material for bioimaging applications, especially upon doping with Cr ion. Cr ions are expected to produce emissions around 700 nm due to d-d type transitions. It has a reported band gap of 3.30 eV (375 nm). In our case, the sample could be prepared at 800 °C with little noticeable unreacted ZnO, cf. Figure 1. We prepared all further samples at this temperature only. The 375 nm band overlaps exactly with the host absorption in ZnO, suggesting that upon changing the ZnO concentration, the band gap of the material can be modified. We decreased ZnO concentration (used as a precursor) firstly in a small step of a change of 0.02 mol in comparison to TiO_2 concentration. The pXRD pattern shows that the reflection due to Zn_2TiO_4 remains unchanged while the signatures due to unreacted ZnO decreases slightly (Figure 2). Upon decreasing ZnO in larger step size (0.20 mol), we observe that Zn_2TiO_4-related reflections remain the same and sample A10 does not show any unreacted ZnO (Figure 3). We performed Rietveld refinement on this sample and observed a very good correlation between experimental and theoretical data (Figure 4). From the SEM results, we confirm that the smaller particles observed in micrographs were due to ZnO, as their concentration decreases with a decrease in the concentration of ZnO (Figure 5). The most interesting observation among all the studies is the change in ZnO-related band in these samples (Figure 11). A part of these results is also shown in Figure 6.

Upon modulating ZnO concentration, we observe a decrease in the ZnO-related band, and for sample A10, the 375 nm band vanishes. The pXRD pattern of Zn_2TiO_4 does not change drastically, and the only change is observed in the unreacted ZnO, which is completely removed now for sample A10. This suggests that the band gap of Zn_2TiO_4 is modified to 4.40 eV (Figure 7). In some reports, the band is also mentioned to be 4.41 eV [18]. This value is in good agreement with our value. The FTIR results suggest that the samples are hygroscopic in nature, and chemistry-related tools should be used to improve performance in this direction (Figure 8). The prominent emission in the samples is in the UV-A region, which can find suitable applications in biomedical applications. The luminescence decay time of this emission is in the 'ns' regime (Figure 9). Sample A10 also shows PersL with a decay time of 15 min, while the TL glow curves indicate that the sample possesses a deep defect of E_{ac} = 1.07 eV (Figure 10). This defect is capable of acting as a reservoir of charges for storage applications.
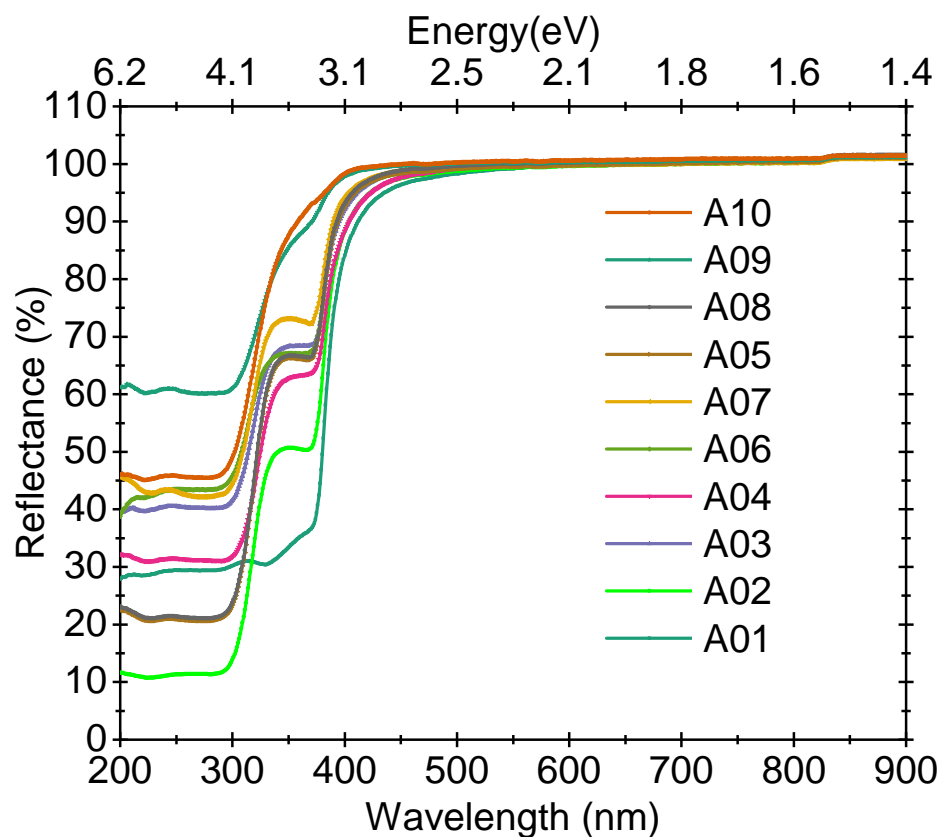
Figure 11. UV-Visible diffuse reflectance spectra of all the samples.

5. Conclusions

Herein, we present a systematic approach to synthesize pure-phase highly crystalline Zn_2TiO_4 samples using the solid-state synthesis method. The sample could be prepared at 800 °C upon annealing for 2 h in an air atmosphere. The small amount of ZnO in the lattice has a tremendous impact on the band gap calculations. In contrast to several reports in the literature, we observe that the band gap of the pure sample is ∼4.40 eV. The crystallite size of the pure sample is around 163 nm. The maximum of the PL excitation band is observed at 225 nm, while the prominent emission is obtained at 346 nm. The decay results suggest that there are at least two relaxation channels for charges to come back to the ground state from an excited state. The present results open a new direction of research, and a similar strategy can be applied to prepare several materials that otherwise require high-temperature annealing conditions and/or processing protocols. If doped with Cr, the material is expected to find an application in bioimaging, paving the way for further research.

Institutional Review Board Statement: Not applicable.

Informed Consent Statement: Not applicable.

Data Availability Statement: The original contributions presented in the study are included in the article, further inquiries can be directed to the corresponding author.

Abbreviations

The following abbreviations are used in this manuscript:

PersL	Persistent Luminescence
PL	Photoluminescence
TL	Thermoluminescence
pXRD	Powder X-ray diffraction
FTIR	Fourier transform infrared
UV	Ultraviolet

References

1. Maldiney, T.; Bessière, A.; Seguin, J.; Teston, E.; Sharma, S.K.; Viana, B.; Bos, A.J.; Dorenbos, P.; Bessodes, M.; Gourier, D.; et al. The in vivo activation of persistent nanophosphors for optical imaging of vascularization, tumours and grafted cells. *Nat. Mater.* **2014**, *13*, 418–426. [CrossRef] [PubMed]

2. Basavaraju, N.; Sharma, S.; Bessière, A.; Viana, B.; Gourier, D.; Priolkar, K.R. Red persistent luminescence in $MgGa_2O_4$: Cr^{3+}; a new phosphor for in vivo imaging. *J. Phys. D Appl. Phys.* **2013**, *46*, 375401. [CrossRef]

3. Ono, T.; Oharu, D.; Kobayashi, S.; Yamada, H.; Takita, S.; Maeda, M.; Takase, K.; Takano, Y.; Watanabe, T. Element substitution effects on magnetic properties of spin-frustrated spinel Znb_2O_4 (B = cr and fe). *Solid State Phenom.* **2017**, *257*, 111–114. [CrossRef]

4. Kim, B.N.; Hiraga, K.; Morita, K.; Sakka, Y. A high-strain-rate superplastic ceramic. *Nature* **2001**, *413*, 288–291. [CrossRef]

5. Zerr, A.; Miehe, G.; Serghiou, G.; Schwarz, M.; Kroke, E.; Riedel, R.; Fueß, H.; Kroll, P.; Boehler, R. Synthesis of cubic silicon nitride. *Nature* **1999**, *400*, 340–342. [CrossRef]

6. Jahren, A.H.; Kruger, M.B.; Jeanloz, R. Alexandrite as a high-temperature pressure calibrant, and implications for the ruby-fluorescence scale. *J. Appl. Phys.* **1992**, *71*, 1579–1582. [CrossRef]

7. Sharma, S.K.; James, J.; Gupta, S.K.; Hussain, S. UV-A,B,C Emitting Persistent Luminescent Materials. *Materials* **2023**, *16*, 236. [CrossRef]

8. Li, L.; Yang, H.; Wang, D.; Feng, G.; Li, B.; Gao, Z.; Xu, D.; Ding, Z.; Liu, X. Large-size and high-quality Zn_2TiO_4 single crystal grown by the optical floating zone method. *J. Cryst. Growth* **2010**, *312*, 3561–3563. [CrossRef]

9. Butee, S.; Kulkarni, A.R.; Prakash, O.; Aiyar, R.; Wattamwar, I.; Bais, D.; Sudheendran, K.; Raju, K.J. Significant enhancement in quality factor of Zn_2TiO_4 with Cu-substitution. *Mater. Sci. Eng. B* **2011**, *176*, 567–572. [CrossRef]

10. Khatua, L.; Panda, R.; Nayak, A.K.; Singh, A.; Sahoo, P.K.; Pradhan, D.; Singh, U.P.; Das, S.K. Efficient UV photocatalytic dye decomposition activity with cost effective solid state reaction grown Zinc Orthotitanate (Zn_2TiO_4) nanoparticles. *J. Alloys Compd.* **2018**, *764*, 895–900. [CrossRef]

11. Pirarath, R.; Bhagwat, U.O.; Palani, S.; Aljafari, B.; Sambandam, A. Nanostructured zinc orthotitanates for photocatalytic removal of dye pollutants. *Mater. Sci. Eng. B* **2023**, *287*, 116107. [CrossRef]

12. Chaves, A.C.; Lima, S.J.; Araújo, R.C.; Maurera, M.A.M.; Longo, E.; Pizani, P.S.; Simões, L.G.; Soledade, L.E.; Souza, A.G.; dos Santos, I.M.G. Photoluminescence in disordered Zn_2TiO_4. *J. Solid State Chem.* **2006**, *179*, 985–992. [CrossRef]

13. Rodríguez-Carvajal, J. Recent advances in magnetic structure determination by neutron powder diffraction. *Phys. B Condens. Matter* **1993**, *192*, 55–69. [CrossRef]

14. Udom, I.; Ram, M.K.; Stefanakos, E.K.; Hepp, A.F.; Goswami, D.Y. One dimensional-ZnO nanostructures: Synthesis, properties and environmental applications. *Mater. Sci. Semicond. Process.* **2013**, *16*, 2070–2083. [CrossRef]

15. Marin, S.J.; O'Keeffe, M.; Partin, D.E. Structures and crystal chemistry of ordered spinels: $LiFe_5O_8$, $LiZnNbO_4$, and Zn_2TiO_4. *IEEE J. Solid-State Circuits* **1994**, *113*, 413–419. [CrossRef]

16. Le, Y.; Luan, C.; Wang, D.; Zhang, B.; Xiao, H.; Ma, J. Characterization and synthesis of cubic Zn_2TiO_4 crystalline films deposited on $MgAl_2O_4$ (100) substrates. *Mater. Lett.* **2021**, *302*, 130395. [CrossRef]

17. Li, L.; Li, F.; Cui, T.; Zhou, Q.; Xu, D. Optical interband transitions in Zn_2TiO_4 single crystals. *Phys. Status Solidi A* **2012**, *209*, 2596–2599. [CrossRef]

18. Zhang, B.; Luan, C.; Wang, D.; Xiao, H.; Feng, X.; Le, Y.; Ma, J. Structural and optical properties of single crystal Zn_2TiO_4 films prepared on MgO (110) substrates. *Ceram. Int.* **2022**, *48*, 4312–4317. [CrossRef]

19. van Rij, L.; Winnubst, L.; Jun, L.; Schoonman, J. Analysis of the preparation of In-doped $CaZrO_3$ using a peroxo-oxalate complexation method. *J. Mater. Chem.* **2000**, *10*, 2515–2521. [CrossRef]

20. James, J.; Sharma, A.; Hussain, S.; Sharma, S.K. Gd Doping-Induced Luminescence Red-Shift in the $CaZrO_3$ Perovskite for Optoelectronics. *ACS Appl. Opt. Mater.* **2023**, *1*, 2042–2048. [CrossRef]

21. Zhang, Y.; Wu, Z.; Geng, D.; Kang, X.; Shang, M.; Li, X.; Lian, H.; Cheng, Z.; Lin, J. Full Color Emission in ZnGa$_2$O$_4$: Simultaneous Control of the Spherical Morphology, Luminescent, and Electric Properties via Hydrothermal Approach. *Adv. Funct. Mater.* **2014**, *24*, 6581–6593. [CrossRef]
22. Xiao, L.-P.; Zeng, L.; Yang, X. Electronic and optical properties of spinel Zn$_2$TiO$_4$ under pressure effect: Ab initio study. *Eur. Phys. J.* **2019**, *92*, 182. [CrossRef]
23. Furetta, C. *Handbook of Thermoluminescence*; World Scientific Pub.: Singapore, 2003. [CrossRef]